CHIN. PHYS. LETT. Vol. 38, No. 8 (2021) 087201

Proximity Effect of Epitaxial Iron Phthalocyanine Molecules on High-Quality Graphene Devices

Haiyang Pan(潘海洋)[1†], Xiaobo Wang(王晓波)[2†], Qiaoming Wang(王巧鸣)[1], Xiaohua Wu(吴小华)[1], Chang Liu(刘畅)[1], Nian Lin(林念)[2*], and Yue Zhao(赵悦)[1,3*]

[1]*Department of Physics, Southern University of Science and Technology, Shenzhen 518055, China*
[2]*Department of Physics, The Hong Kong University of Science and Technology, Hong Kong, China*
[3]*Shenzhen Institute for Quantum Science and Engineering, Southern University of Science and Technology, Shenzhen 518055, China*

(Received 13 May 2021; accepted 26 June 2021; published online 2 August 2021)

Depositing magnetic insulators on graphene has been a promising route to introduce magnetism via exchange proximity interaction in graphene for future spintronics applications. Molecule-based magnets may offer unique opportunities because of their synthesis versatility. Here, we investigate the magnetic proximity effect of epitaxial iron phthalocyanine (FePc) molecules on high-quality monolayer and bilayer graphene devices on hexagonal boron nitride substrates by probing the local and nonlocal transport. Although the FePc molecules introduce large hole doping effects combined with mobility degradation, the magnetic proximity gives rise to a canted antiferromagnetic state under a magnetic field in the monolayer graphene. On bilayer graphene and FePc heterostructure devices, the nonlocal transport reveals a pronounced Zeeman spin-Hall effect. Further analysis of the scattering mechanism in the bilayer shows a dominated long-range scattering. Our findings in graphene/organic magnetic insulator heterostructure provide a new insight for use of molecule-based magnets in two-dimensional spintronic devices.

DOI: 10.1088/0256-307X/38/8/087201

Graphene possesses unusual electronic properties of high carrier mobility, long spin relaxation distance, and lifetime, providing an attractive prototype gate tunable platform for the manipulation of spin towards next-generation spin-based logic devices.[1−4] The generation of spin-polarized current is usually initialized by spin injection from ferromagnetic electrodes, where the contact interfaces could limit the spin injection efficiency.[3] The unique band structure of graphene allows alternative approaches to creating spin transport without magnetic contacts by introducing magnetism in graphene.[5] The strong hybridization of graphene and magnetic materials can generate proximity-induced spin polarization and exchange splitting to the electronic structure of graphene. Direct adsorption of magnetic atoms or molecular magnets is expected to introduce proximity-induced magnetism effects in graphene.[6−10] However, the magnetic dopants can also act as impurities scattering centers, resulting in mobility degradation and doping effects, thus impacting electrical transport performance.[11−14] Bringing graphene in contact with ferromagnetic insulators has been considered in a promising step to introduce a magnetic exchange field for spin-polarized edge conduction. Magnetic proximity effects induced strong Zeeman splitting have been observed in several graphene/magnetic insulator heterostructure systems, including EuS films, $CrBr_3$ thin layers, and $BiFeO_3$ nanoplates.[5,15−18]

Despite the recent progress, there has been little investigation of graphene heterostructure devices with molecular-based magnets. Transition metal phthalocyanines have been known as organic magnetic semiconductors where their magnetic properties can be sensitive to the crystal phase of the π-conjugated polymers, depending on the metal ion and orbital overlap.[19] They are cost-effective and easily procurable organic materials. The magnetic molecules exhibit localized electronic spin states with long coherence time and are thus suitable for hybridization with nonmagnetic films to induce spin transport in versatile two-dimensional organic spin interface architectures.[20,21] Driven by the π–π interaction, the polymers can form stable crystalline phase on graphene, offering an integrated graphene/organic ferromagnet interface for investigation of magnetic proximity effect.

Previous work demonstrated that large-scale ordered flat islands of iron (Ⅱ) phthalocyanine (FePc) molecules could be formed on graphene when submonolayer amounts of molecules were deposited.[22] The epitaxial film stabilized by intermolecular non-

Supported by the National Natural Science Foundation of China (Grant No. 11674150), the Key-Area Research and Development Program of Guangdong Province (Grant No. 2019B010931001), the Guangdong Innovative and Entrepreneurial Research Team Program (Grant No. 2016ZT06D348), the SUSTech CRF, and the Hong Kong RGC (Grant Nos. 16300617 and C6012-17E).
†H. Pan and X. Wang contributed equally to this work.
*Corresponding authors. Email: phnlin@ust.hk; zhaoy@sustech.edu.cn
© 2021 Chinese Physical Society and IOP Publishing Ltd

covalent interactions with the graphene surface can form periodic square patterns of FePc molecules with a lattice constant of 1.4 nm. The absence of inhomogeneous cluster formation also mitigates additional disorder scattering in the transport properties of graphene. The bulk material of FePc molecules exhibits ferromagnetic order with T_c around 10 K.[19] For FePc thin films, its properties are related to the deposition substrate. The magnetization measurements and x-ray magnetic circular dichroism results reveal that the FePc thin films on gold surface exhibit ferromagnetic order in the molecule plane below 4.5 K.[19]

In the present study, we investigate the magnetic proximity effect of epitaxially grown FePc films on monolayer and bilayer graphene by comparing the local and nonlocal transport measurements. To minimize charge impurity scattering and improve carrier mobility, we transfer graphene on hexagonal boron nitride (h-BN) for high-quality electrical properties.[23,24] Our measurements show that the magnetic proximity effect from FePc deposition creates different ground states on monolayer and bilayer graphene devices. On monolayer graphene, the nonlocal measurements show a suppressed peak near the charge neutrality point under a magnetic field, while the local transverse resistance remains high, indicating the formation of a canted antiferromagnetic (CAFM) state from the magnetic proximity effect. On bilayer graphene, we observe a reducing local resistance and an increasing nonlocal resistance at the Dirac point as the magnetic field increases, consistent with the formation of a Zeeman spin Hall effect. By analyzing the ratio of transport scattering time (τ_t) to quantum scattering time (τ_q) in bilayer graphene/FePc heterostructure, we believe that the transport properties are dominated by long-range charge impurity scattering.

Results and Discussion. Figure 1(a) shows the molecular structure of FePc, where one Fe atom is connected with four pyrrolic N atoms in square-planar coordination. These planar molecules formed linear chains by columnar stacking in the thin films. The monolayer of FePc molecules deposited on the graphene surface formed a well-ordered flat array. Figure 1(c) shows the scanning tunneling microscopy (STM) topography image of a FePc monolayer on HOPG. The planes of FePc molecules are parallel to the substrate, similar to the structure of FePc on a gold substrate,[19] where the magnetization measurements show a small coercive field (only a few hundreds of gauss) and a ferromagnetic order with an in-plane easy axis and a slightly tilted magnetic moment from the molecular plane. After verifying the array-order of our FePc film, more than one layer of FePc molecules are deposited onto the surface of the G/BN devices to ensure the coverage and the magnetic interface. The deposition of FePc was performed at an ultra-high vacuum environment with *in situ* vacuum annealing of the G/BN devices so that the atomic contact at the interface can be guaranteed.

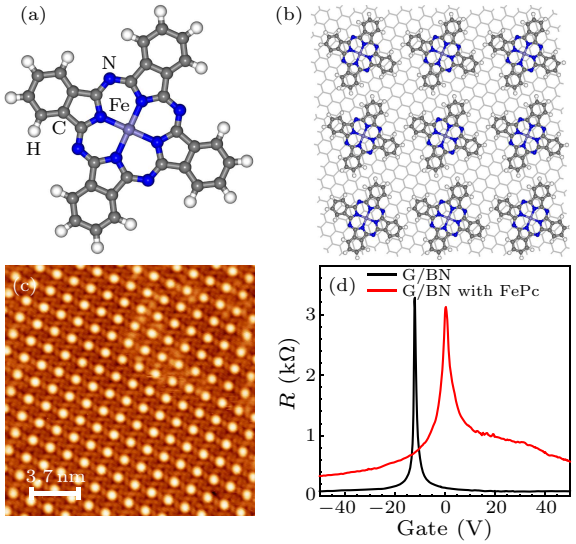

Fig. 1. FePc molecule structure and characterization. (a) Structure of FePc molecule. (b) DFT calculated structure of FePc molecules on graphene surface. (c) A scanning tunneling microscopy (STM) image (tunneling parameters: 200 mV, 0.52 nA) of the FePc molecules adsorbed in a squared closed-packed geometry on the graphite surface. The scale bar is 3.7 nm. (d) Resistance versus applied back gate voltage for monolayer graphene before and after FePc molecules deposition measured at 1.6 K.

Figure 1(d) presents the gate voltage (V_g) dependent resistance for a typical monolayer graphene device before and after FePc deposition. After the FePc deposition, the monolayer graphene device experiences a rightwards shift of charge neutrality point and a broadened Dirac peak, implying a hole doping effect and impurity scattering by the organic molecule. The FePc film introduces an initial hole doping on the level of $8.7 \times 10^{11}\,\mathrm{cm}^{-2}$. The mobility, obtained by fitting the relation between conductivity (σ) and the carrier density (n) (Fig. S3 in the Supporting Information), decreases by one order from $139000\,\mathrm{cm}^2\cdot\mathrm{V}^{-1}\cdot\mathrm{s}^{-1}$ to $14000\,\mathrm{cm}^2\cdot\mathrm{V}^{-1}\cdot\mathrm{s}^{-1}$. Charge inhomogeneity δn calculated from the width of the Dirac peak increases from $7.0 \times 10^{10}\,\mathrm{cm}^{-2}$ to $4.8 \times 10^{11}\,\mathrm{cm}^{-2}$. Similar hole doping and mobility degradation were observed in bilayer devices, as shown in Fig. S2. In addition, the conductivity curves $\sigma(n)$ for both the monolayer and bilayer devices (Fig. S3) exhibit behavior change from sublinear to linear after FePc deposition, consistent with a dominant charge impurity scattering caused by the inhomogeneous charge doping from the adjacent FePc molecules.[12,25–28] Density functional theory (DFT) calculations on the band structure of the FePc/monolayer graphene (FePc/MG) heterostructure (Fig. S6) shows an additional state contributed from the Fe 3*d* orbital near the Dirac cone

at the Γ point, which may contribute to the electron-hole asymmetry behavior of the monolayer graphene device after the FePc deposition.

When the magnetic order is formed in the FePc film at $T < T_c$, the strong exchange field is expected to result in a Zeeman splitting effect in graphene, as shown in Fig. 2(a). The spin degeneracy at the charge neutrality point can be lifted, leading to sub-bands with opposite spin due to the Zeeman splitting. When the Fermi level lies between the sub-band Dirac points, both spin-up holes and spin-down electrons exist. Under external magnetic field, as illustrated in Fig. 2(b), an enhanced nonlocal signal can be observed near the Dirac point due to the Zeeman splitting with a ferromagnetic (FM) ground phase.[15,16,29–32]

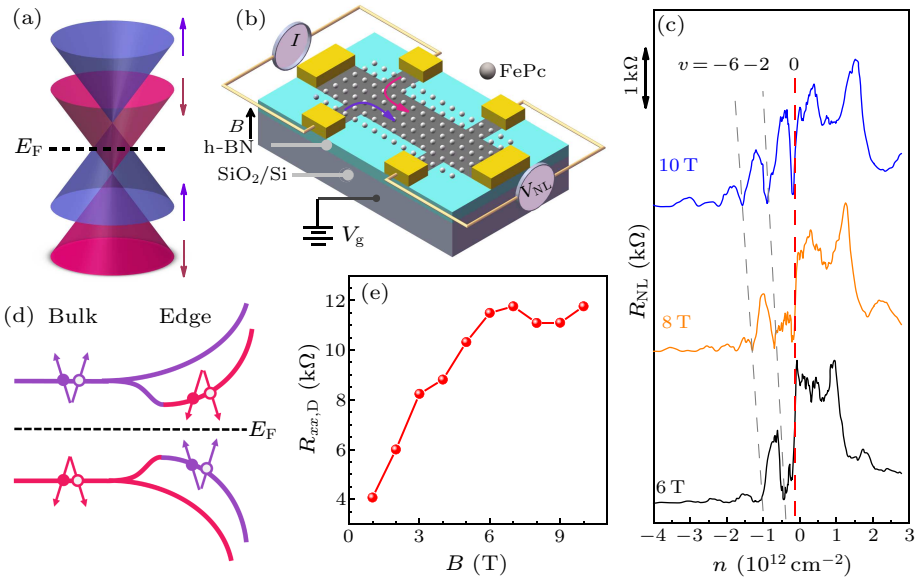

Fig. 2. Electrical transport of monolayer graphene with FePc molecules at 1.6 K. (a) The schematic of the Zeeman splitting of the Dirac cone in monolayer graphene. (b) The electrodes configuration schematic of nonlocal measurements. The black Hall bar represents graphene layer. (c) Nonlocal curves of monolayer G/BN device with FePc molecular film measured at 6 T, 8 T and 10 T. (d) Simplified schematic of the canted antiferromagnetic phase with a gap opening on the helical edge states, where the spectrum contains four branches related to the spin and valley degeneracies. The arrows with different colors (red and purple) denote the lifting of spin degeneracy. (e) The longitudinal resistance $R_{xx,D}$ at the Dirac point versus applied magnetic field.

Figure 2(c) presents the gate dependent nonlocal resistance as a function of carrier density of the FePc/MG device under different magnetic fields at $T = 1.6$ K. A dip in the nonlocal resistance appears near the Dirac point when the magnetic field approaches 8 T. As magnetic field increases, the dip of filling factors $v = 0$ becomes more prominent with an almost vanishing nonlocal resistance. On the other hand, the local transport measurement shows that the local resistance at the Dirac peak increases with an external magnetic field and tends to saturate at $B > 7$ T [Fig. 2(e)]. The nonlocal resistance dip and saturated local resistance at the Dirac peak are in sharp contrast to the formation of gapless spin-polarized edge channels due to the Zeeman spin Hall effect, where an increase of nonlocal resistance and a decrease of local resistance with magnetic field are expected. The exchange field (B_{exc}) introduced by the magnetic proximity effect from FePc gives rise to Zeeman splitting for the symmetry broken zero-energy Landau level.[33–35] When an external magnetic field is applied, both valley isospin anisotropy energy ($\propto B_\perp$) and Zeeman energy ($\propto B_{exc} + B_\perp$) increases.[16,33] The competition between valley isospin anisotropy energy and Zeeman energy can lead to different ground states. A gapless spin-polarized ferromagnetic state is preferred when Zeeman energy is much larger than valley isospin anisotropy energy. On the other hand, when Zeeman energy is comparable to valley isospin anisotropy energy, the formation of a canted antiferromagnetic (CAFM) state brings an edge gap.[36,37] As shown in the schematic diagram of the CAFM state [Fig. 2(d)], the opening of an edge state gap can effectively decrease the nonlocal signal and enhance longitudinal resistance at the Dirac point ($R_{xx,D}$). These observed local and nonlocal behaviors near Dirac point at high field are consistent with CAFM ground state. There is a saturation behavior of $R_{xx,D}$ at $B > 7$ T, possibly due to the disorder scattering from the neighboring FePc molecules.

We then investigate the proximity effect of the FePc film on bilayer graphene. Figures 3(a) and 3(b) show the nonlocal and local resistance as a function of carrier density for a bilayer graphene/FePc (FePc/BG) heterostructure device. As summarized in Fig. 3(c), when the magnetic field increases, the

nonlocal peak value $R_{\mathrm{NL,D}}$ keeps increasing from 0 to 10 T. In comparison, the local resistance peak increases first ($0 < B < 2$ T), then quickly decreases ($2\,\mathrm{T} < B < 10$ T). The associated local and nonlocal transport behaviors above 2 T are consistent with a ground state ($v = 0$) phase of the ferromagnetic (FM) state because of the magnetic proximity effect from the FePc film. Figure 3(d) shows the schematics of the FM phases for bilayer graphene based on the quantum Hall ferromagnetism theory.[33–35] Due to the extra orbital degeneracy of the zero-energy Landau level in bilayer graphene, the number of branches is doubled compared to monolayer graphene. We focus mainly on the evolution of spin-polarized edge channels. The edge gap closes at the FM phase, and there exist gapless counter-propagating edge channels with opposite spins, leading to a decrease of $R_{xx,\mathrm{D}}$ and an increase of $R_{\mathrm{NL,D}}$. We note that local peak value $R_{xx,\mathrm{D}}$ increases first from 0 T to 2 T before the FM phase emerges. The onset of FM phase at 2 T may be related to the hole doping effect of the FePc layer. The displacement field introduced by the deposition of FePc could result in layer polarization, leading to a competition among the eight-fold degeneracy breaking at the zero-energy Landau level at a lower magnetic field.[38] The analysis of ohmic contribution (Fig. S7) shows negligible ohmic leakage compared with the nonlocal signal. In bilayer graphene, the displacement field can break the inversion symmetry and introduce the valley Hall effect, giving responses in the local and nonlocal transport signal.[39,40] However, in our case, the displacement field introduced by FePc is relatively small (∼0.08 V/nm) to fully polarize the layer symmetry, indicating displacement field induced valley current is a less likely scenario for the nonlocal transport behavior at high magnetic field. The temperature-dependent $R_{\mathrm{NL,D}}$ at 4 T (Fig. S8) shows a transition around 15 K, which is very close to $T_{\mathrm{c}} \sim 10$ K of bulk FePc (our final deposition thickness is about half a micron), confirming the magnetic proximity effect from the FePc film.

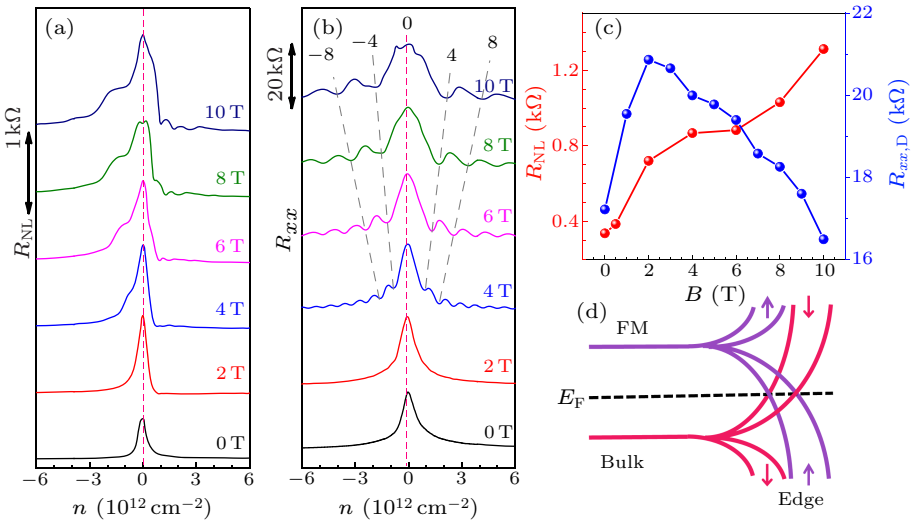

Fig. 3. Zeeman spin Hall effect in bilayer G/BN with FePc film. (a) The nonlocal R_{NL} and (b) longitudinal resistance R_{xx} versus carrier density at different fields. All measurements were performed at 1.6 K. (c) The amplitude of R_{NL} and R_{xx} at Dirac point versus magnetic field. (d) Simplified schematics of the ferromagnetism (FM) state in bilayer graphene. The spectrum contains eight branches related to the spin, valley, and orbital degeneracies. The lifting of spin degeneracy is denoted as purple and red colors. The edge is in a gapless state with counter-propagating spin-polarized edge channels.

To further elucidate the influence of the FePc film on the electron transport properties of bilayer graphene, we conduct Shubnikov-de Haas (SdH) oscillation analysis to reveal the scattering mechanism. The magnetoresistance transport results of the original bilayer graphene are displayed in Fig. 4(a). A prominent SdH oscillation could be observed at various gate voltages, where the oscillation frequency can be obtained by fast Fourier transform (FFT). Figure 4(b) displays the magnetoresistance results of the FePc/BG device. The carrier-density-dependent frequency curves (Fig. S11) before and after FePc deposition were almost identical, indicating the negligible influence of FePc on the Fermi surface size.

The effective mass can be extracted (Fig. S10) from the SdH oscillations by fitting the formula:[1]

$$\frac{A(T)}{A(T_0)} = \frac{T\sinh(2\pi^2 k_{\mathrm{B}} T_0 m^*/\hbar e B_n)}{T_0 \sinh(2\pi^2 k_{\mathrm{B}} T m^*/\hbar e B_n)},$$

where $A(T)$ and $A(T_0)$ are the FFT amplitudes of the SdH oscillations at temperatures T and T_0, respectively, and B_n is the magnetic field corresponding to the peaks of the oscillations. The quantum scattering time (τ_{q}) and transport scattering time ($\tau_{\mathrm{t}} = m^*\mu/e$), before and after the FePc deposition, can be determined, as shown in Figs. 4(c) and 4(d). Calculation

details of τ_q can be found in the Supporting Information. The τ_q of the original graphene ranges from 80 to 130 fs, larger than the reported value in the bilayer graphene on a SiO_2 substrate.[41] The τ_q slightly decreases to 40–100 fs after FePc deposition. The transport scattering time τ_t also decreases from ∼500 fs to less than 200 fs after the deposition.

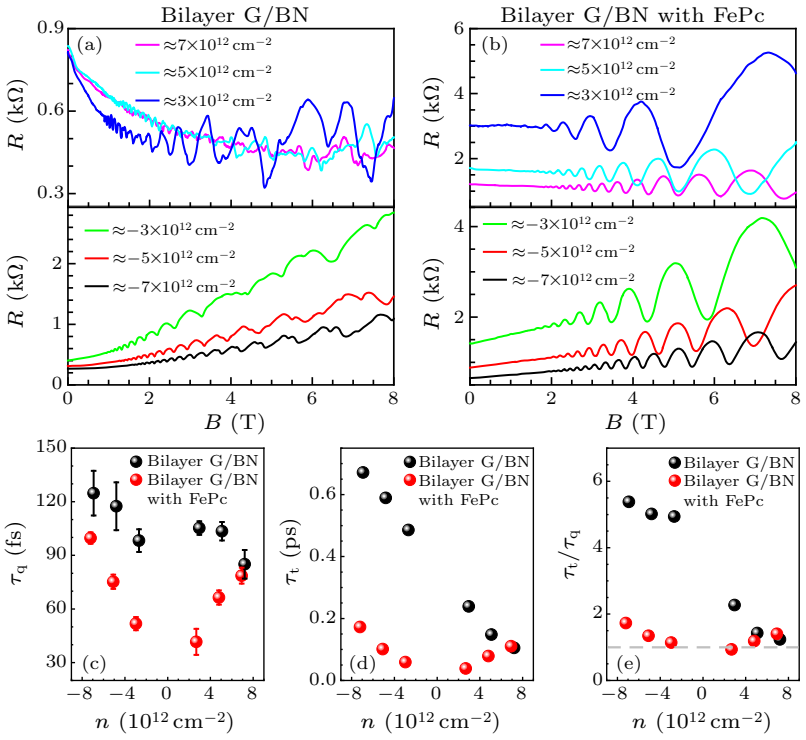

Fig. 4. SdH oscillation and scattering mechanism analysis of the bilayer G/BN device before and after FePc deposition. (a) and (b) The magnetoresistance of the bilayer device without (a) and with (b) FePc film measured at various carrier densities, at $T = 1.6$ K. (c) Quantum scattering time (τ_q) of the bilayer device at various carrier densities without and with the FePc film. (d) Transport scattering time (τ_t) of the bilayer device without and with the FePc film. (e) The ratio of τ_t/τ_q versus carrier density without and with the FePc film.

The ratio of τ_t/τ_q can be a powerful indicator of the complex scattering sources in 2D electron systems.[41] While $\tau_t/\tau_q \sim 1$ indicates wide-angle scattering (related to the short-ranged scattering source), a larger τ_t/τ_q could result from small-angle scattering (related to the long-range charged impurity scattering). Figure 4(e) displays the τ_t/τ_q ratio of the bilayer graphene device before and after FePc deposition. Before FePc deposition, the τ_t/τ_q values ($\tau_t/\tau_q > 4$ on the hole side and $1 < \tau_t/\tau_q < 3$ on the electron side) are in agreement with the reported values for graphene on the SiO_2 substrate, suggesting long-range Coulomb disorder scattering originated from the graphene/substrates interface. After FePc deposition, however, τ_t/τ_q values show a significant decrease, ranging from 0.9 and 1.7. Such a decrease is related to the increased short-range scattering from the magnetic impurities induced by FePc molecules.

In summary, we have systematically investigated local and nonlocal transport properties of monolayer and bilayer graphene devices with epitaxial FePc films. The magnetic proximity effect from the FePc films results in a Zeeman splitting field. A canted antiferromagnetic ground state is observed on monolayer graphene, and a pronounced Zeeman Hall effect is realized on bilayer graphene. Our results reveal the magnetic proximity effect at the interface of graphene/organic magnetic insulator heterostructures and provide a new insight for using molecule-based magnets in two-dimensional spintronic devices.

Methods. The graphene/h-BN (G/BN) samples were prepared using the dry transfer method.[42–44] Graphene pieces were obtained by mechanical exfoliation on polymer methyl methacrylate (PMMA) substrates. h-BN flakes with thicknesses of 20–40 nm were exfoliated on oxidized Si wafers. Mono and bilayer graphene pieces were identified by initial optical microscopy and subsequent Raman spectroscopy. The selected graphene pieces were dry-transferred onto the target h-BN flakes using a transfer station. The G/BN heterostructures were then annealed in an argon and hydrogen atmosphere at 350℃ for three hours to remove the polymer residue.[44] We then selected the graphene areas free from bubbles and wrinkles by atomic force microscopy, where standard electron beam lithography (EBL) and metal evaporation were performed for standard Hall-bar devices. Secondary EBL and reactive ion etching were employed to etch

the rest part. The final devices were reannealed in a mixed argon and hydrogen atmosphere to remove the resist residual.

The FePc molecules purchased from Sigma–Aldrich with the dye content 90% were purified in the ultra-high vacuum (UHV) chamber for several cycles through heating. Those molecules were then loaded into an organic molecular beam epitaxy (OMBE) system and out-gassed for several hours before deposition. The G/BN devices were transferred into the OMBE chamber and annealed at 220℃ for ten hours to remove any organic and moisture residue. The deposition of FePc film occurred at an evaporation temperature of 380℃, while the devices were maintained at 135℃ to optimize the crystallite size. STM characterization was carried out in a CreaTec UHV STM system working at 78 K. The growth rate was 1.1 Å/s, and the estimated thickness of the final film was approximately 462 nm.

The transport measurements were performed in a He^4 cryostat system (Oxford Equipment). The four-probe local and nonlocal measurements were performed using a standard lock-in technique with an AC excitation current of 100 nA. A Keithley source meter (K2400) was applied to the bottom of the SiO_2 (285 nm)/ p-Si substrate as the gate voltage.

References

[1] Novoselov K S, Geim A K, Morozov S V, Jiang D, Katsnelson M I, Grigorieva I V, Dubonos S V and Firsov A A 2005 *Nature* **438** 197
[2] Zhang Y, Tan Y W, Stormer H L and Kim P 2005 *Nature* **438** 201
[3] Tombros N, Jozsa C, Popinciuc M, Jonkman H T and van Wees B J 2007 *Nature* **448** 571
[4] Gmitra M and Fabian J 2017 *Phys. Rev. Lett.* **119** 146401
[5] Wang Z, Tang C, Sachs R, Barlas Y and Shi J 2015 *Phys. Rev. Lett.* **114** 016603
[6] Ding J, Qiao Z, Feng W, Yao Y and Niu Q 2011 *Phys. Rev. B* **84** 195444
[7] Qiao Z, Yang S A, Feng W, Tse W K, Ding J, Yao Y, Wang J and Niu Q 2010 *Phys. Rev. B* **82** 161414
[8] Qiao Z, Jiang H, Li X, Yao Y and Niu Q 2012 *Phys. Rev. B* **85** 115439
[9] Candini A, Klyatskaya S, Ruben M, Wernsdorfer W and Affronte M 2011 *Nano Lett.* **11** 2634
[10] Jin Y J L, Lin L and Zhu J J 2020 *Chin. Phys. Lett.* **37** 087501
[11] McCreary K M, Swartz A G, Han W, Fabian J and Kawakami R K 2012 *Phys. Rev. Lett.* **109** 186604
[12] Chen J H, Jang C, Adam S, Fuhrer M S, Williams E D and Ishigami M 2008 *Nat. Phys.* **4** 377
[13] Cai C Y and Chen J H 2018 *Chin. Phys. B* **27** 67304
[14] Qin Y, Wang S, Wang R, Bu H, Wang X, Wang X, Song F, Wang B and Wang G 2016 *Appl. Phys. Lett.* **108** 203106
[15] Wei P, Lee S, Lemaitre F, Pinel L, Cutaia D, Cha W, Katmis F, Zhu Y, Heiman D, Hone J, Moodera J S and Chen C T 2016 *Nat. Mater.* **15** 711
[16] Wu Y F, Song H D, Zhang L, Yang X, Ren Z, Liu D, Wu H C, Wu J, Li J G, Jia Z, Yan B, Wu X, Duan C G, Han G, Liao Z M and Yu D 2017 *Phys. Rev. B* **95** 195426
[17] Tang C, Zhang Z, Lai S, Tan Q and Gao W B 2020 *Adv. Mater* **32** 1908498
[18] Wu Y, Cui Q, Zhu M, Liu X, Wang Y, Zhang J, Zheng X, Shen J, Cui P, Yang H and Wang S 2021 *ACS Appl. Mater. Interfaces* **13** 10656
[19] Gredig T, Colesniuc C N, Crooker S A and Schuller I K 2012 *Phys. Rev. B* **86** 014409
[20] Avvisati G, Cardoso C, Varsano D, Ferretti A, Gargiani P and Betti M G 2018 *Nano Lett.* **18** 2268
[21] Gamou H, Shimose K, Enoki R, Minamitani E, Shiotari A, Kotani Y, Toyoki K, Nakamura T, Sugimoto Y, Kohda M, Nitta J and Miwa S 2020 *Nano Lett.* **20** 75
[22] de la T B, Švec M, Hapala P, Redondo J, Krejčí O, Lo R, Manna D, Sarmah A, Nachtigallová D, Tuček J, Błoński P, Otyepka M, Zbořil R, Hobza P and Jelínek P 2018 *Nat. Commun.* **9** 2831
[23] Dean C R, Young A F, Meric I, Lee C, Wang L, Sorgenfrei S, Watanabe K, Taniguchi T, Kim P, Shepard K L and Hone J 2010 *Nat. Nanotechnol.* **5** 722
[24] Zomer P J, Dash S P, Tombros N and Wees B J V 2011 *Appl. Phys. Lett.* **99** 232104
[25] Hwang E H, Adam S and Sarma S D 2007 *Phys. Rev. Lett.* **98** 186806
[26] Tan Y W, Zhang Y, Bolotin K, Zhao Y, Adam S, Hwang E H, Das S S, Stormer H L and Kim P 2007 *Phys. Rev. Lett.* **99** 246803
[27] Wehling T O, Yuan S, Lichtenstein A I, Geim A K and Katsnelson M I 2010 *Phys. Rev. Lett.* **105** 056802
[28] Li C, Komatsu K, Bertrand S, Clavé G, Campidelli S, Filoramo A, Guéron S and Bouchiat H 2016 *Phys. Rev. B* **93** 045403
[29] Abanin D A, Morozov S V, Ponomarenko L A, Gorbachev R V, Mayorov A S, Katsnelson M I, Watanabe K, Taniguchi T, Novoselov K S, Levitov L S and Geim A K 2011 *Science* **332** 328
[30] Avsar A, Tan J Y, Taychatanapat T, Balakrishnan J, Koon G K W, Yeo Y, Lahiri J, Carvalho A, Rodin A S, O'Farrell E C T, Eda G, Castro N A H and Özyilmaz B 2014 *Nat. Commun.* **5** 4875
[31] Wojtaszek M, Vera-Marun I J, Maassen T and van Wees B J 2013 *Phys. Rev. B* **87** 081402
[32] Ribeiro M, Power S R, Roche S, Hueso L E and Casanova F 2017 *Nat. Commun.* **8** 2198
[33] Kharitonov M 2012 *Phys. Rev. B* **85** 155439
[34] Kharitonov M 2012 *Phys. Rev. B* **86** 075450
[35] Nomura K and MacDonald A H 2006 *Phys. Rev. Lett.* **96** 256602
[36] Young A F, Sanchez-Yamagishi J D, Hunt B, Choi S H, Watanabe K, Taniguchi T, Ashoori R C and Jarillo-Herrero P 2014 *Nature* **505** 528
[37] Li Y, Amado M, Hyart T, Mazur G P, Risinggård V, Wagner T, McKenzie-Sell L, Kimbell G, Wunderlich J, Linder J and Robinson J W A 2020 *Phys. Rev. B* **101** 241405
[38] McCann E 2006 *Phys. Rev. B* **74** 161403
[39] Shimazaki Y, Yamamoto M, Borzenets I V, Watanabe K, Taniguchi T and Tarucha S 2015 *Nat. Phys.* **11** 1032
[40] Sui M, Chen G, Ma L, Shan W Y, Tian D, Watanabe K, Taniguchi T, Jin X, Yao W, Xiao D and Zhang Y 2015 *Nat. Phys.* **11** 1027
[41] Hong X, Zou K and Zhu J 2009 *Phys. Rev. B* **80** 241415
[42] Wang J I J, Yang Y, Chen Y A, Watanabe K, Taniguchi T, Churchill H O H and Jarillo-Herrero P 2015 *Nano Lett.* **15** 1898
[43] Dean C R, Young A F, Cadden-Zimansky P, Wang L, Ren H, Watanabe K, Taniguchi T, Kim P, Hone J and Shepard K L 2011 *Nat. Phys.* **7** 693
[44] Pan H, Wang Q, Wu X, Song T, Song Q and Wang J 2020 *Nanotechnology* **31** 355001

Supporting Information for "**Proximity Effect of Epitaxial Iron Phthalocyanine Molecules on High-Quality Graphene Devices**"

Haiyang Pan[1*], Xiaobo Wang[2*], Qiaoming Wang[1], Xiaohua Wu[1], Chang Liu[1], Nian Lin[2†], and Yue Zhao[1,3‡]

[1]Department of Physics, Southern University of Science and Technology, Shenzhen 518055, China

[2]Department of Physics, The Hong Kong University of Science and Technology, Hong Kong, China

[3]Shenzhen Institute for Quantum Science and Engineering, Southern University of Science and Technology, Shenzhen 518055, China

Raman spectroscopy of the FePc molecules

The Raman spectrum of the FePc molecules on the molybdenum (Mo) substrate is shown in Figure S1. The appearance of multiple resonant vibrating peaks represents the varying vibrating modes of FePc molecules.[1]

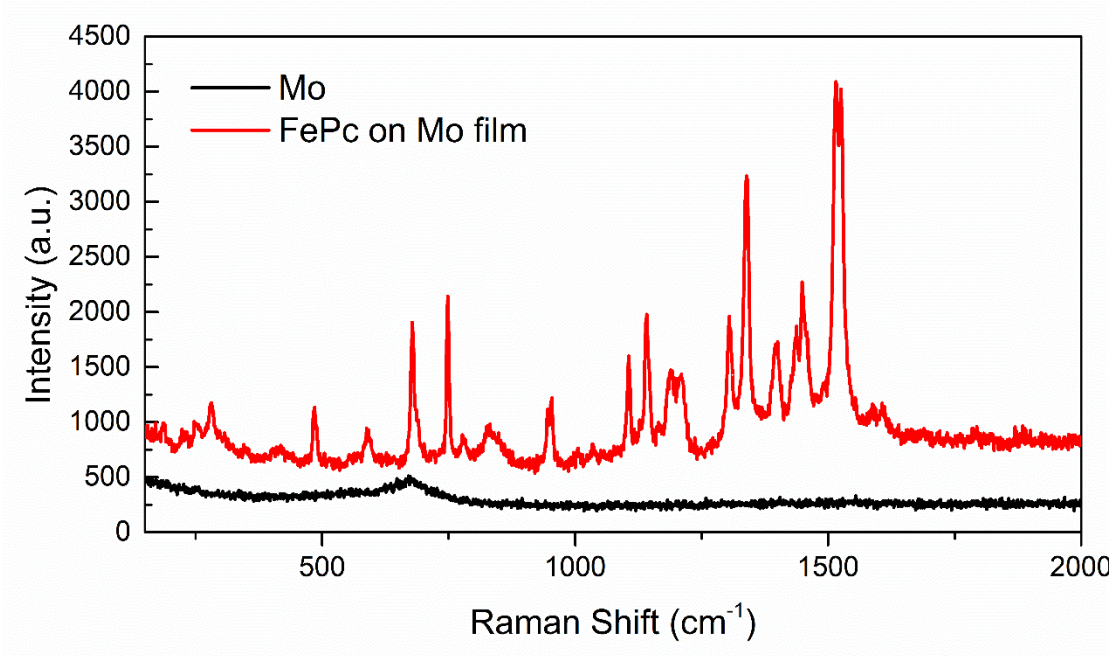

Figure S1 The Micro-Raman spectra of the molybdenum polycrystal substrate (black curve) and the FePc molecules deposited on the Mo substrate (red curve).

The influence of FePc film on the transport properties of bilayer graphene

The resistance versus gate voltage curves of bilayer graphene before (original) and after (modified) FePc deposition are shown in Figure S2. Similar to monolayer graphene, the bilayer graphene device also exhibits a rightward shift of charge-neutral point (V_D) and a broadening of Dirac peak after FePc deposition.

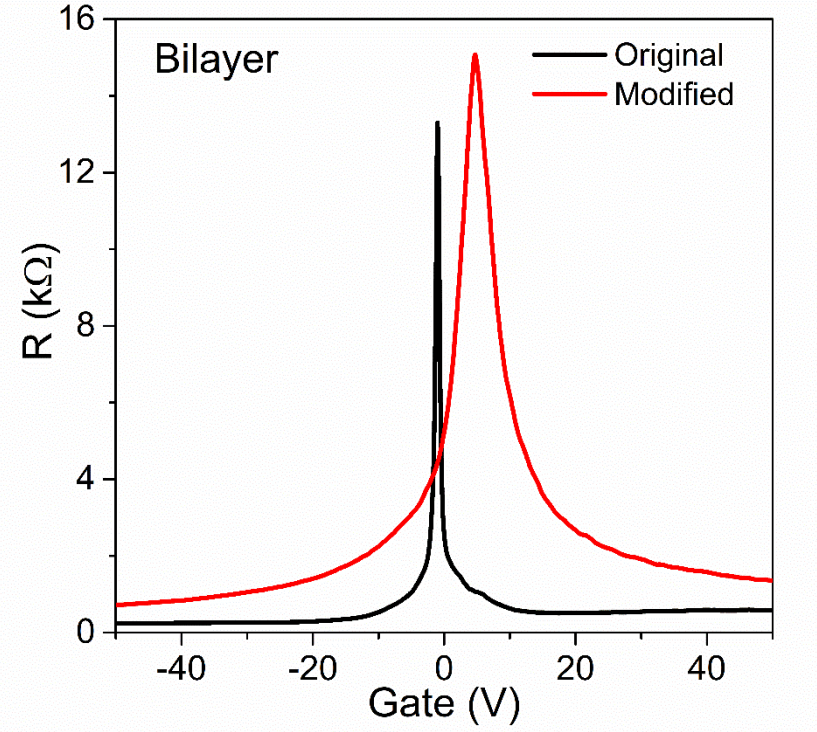

Figure S2 Longitudinal resistance versus back gate voltage of bilayer G/BN device before and after FePc deposition at T = 1.6 K.

The displacement field induced by the FePc layer could be roughly estimated by the CNP shift. The back gate CNP shifted less than 10 V (~ 300 nm SiO2 and ~ 30 nm hBN) in both the mono and bilayer device, as shown in Fig. 1d and Fig. S2. To introduce such a hole doping effect $n = \varepsilon_0 D_{FePc}$, the displacement field felt by the bilayer graphene from FePc can then be calculated $D_{FePc} = D_{backgates\ hift} = \frac{\varepsilon_b (V_{backgates\ \ hift})}{d_b}$ ~0.08 V/nm (ε_{SiO2}~4, ε_{BN}~4, $V_{backgates\ hift}$~6.5 V). Since the original bilayer device is of high quality with CNP around zero, the displacement field induced by FePc layer(~ 0.08V/nm) could be insufficient to fully polarize the layer symmetry.

Mobility analysis

The carrier-density dependent conductivity (σ) is shown in Fig. S3. The carrier density is calculated by $n = \alpha (V_g\text{-}V_D)$, where α is the capacitance factor calibrated by Hall measurement.[2] To analyze the change in device mobility (μ), we fit the conductivity curve by $1/\sigma = 1/(ne\mu + \sigma_0) + \rho_s$, where σ_0 is the residual conductivity at the charge neutrality point and ρ_s is a resistivity constant from short-range scattering.[2, 3] For the monolayer device, we obtained μ = 138,560 $cm^2V^{-1}s^{-1}$, ρ_s = 51 Ω for before the deposition and μ = 13,560 $cm^2V^{-1}s^{-1}$, ρ_s = 139 Ω after the deposition. For the bilayer device, the fitting gave μ = 25,780 $cm^2V^{-1}s^{-1}$, ρ_s = 133 Ω before the deposition, and μ = 1,900 $cm^2V^{-1}s^{-1}$, ρ_s = 57 Ω after the deposition.

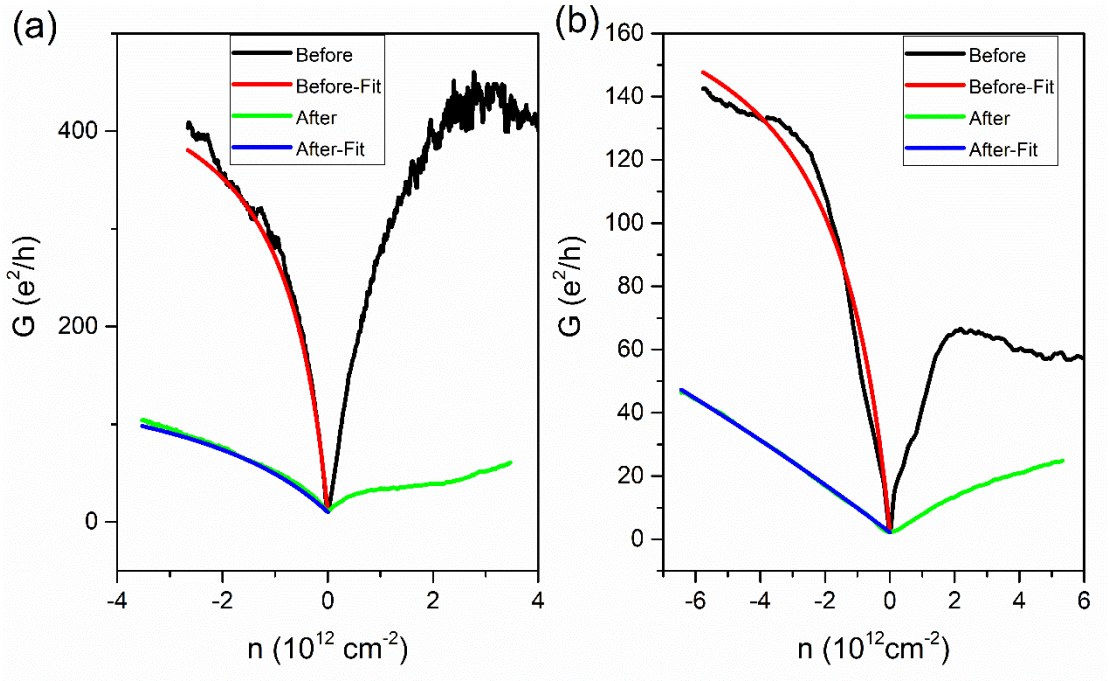

Figure S3 The carrier density dependence of the conductivity curves. (a) The original and modified conductivity curves for monolayer G/BN. (b) The original and modified conductivity curves for bilayer G/BN.

The nonlocal resistance of the original monolayer G/BN device

The typical R_{NL} curves of G/BN without FePc molecules are showed in Figure S4. The prominent nonlocal peak near Dirac point can be seen. Other dip peaks also exist when the carrier density is increased, which can be attributed to the standard quantum

Hall edge-state transport originating from the lifting of landau level degeneracy.

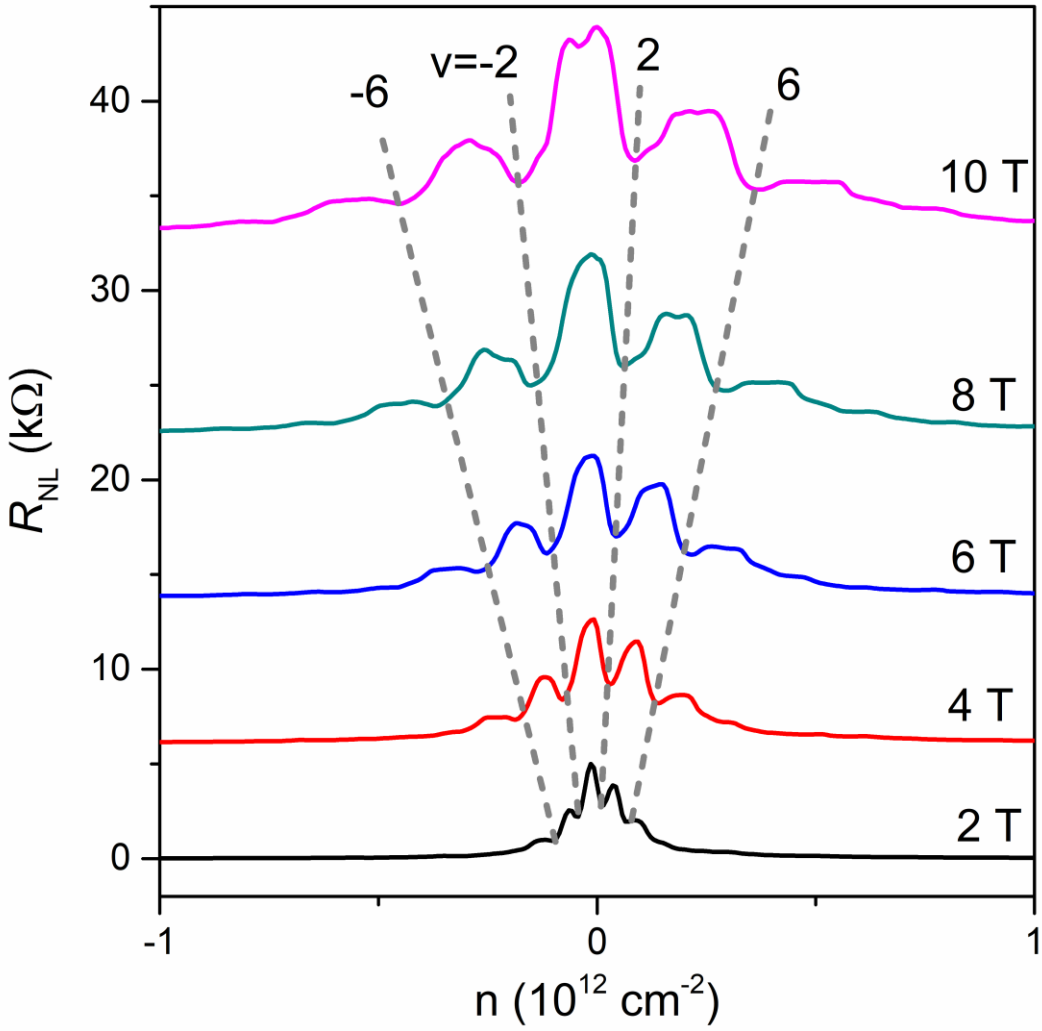

Figure S4 Typical nonlocal curves of monolayer G/BN device without FePc deposition.

The local measurement of the monolayer G/BN device after FePc film deposition

In our monolayer G/BN system, the measured R_{xx} and R_{xy} vs. B are plotted in Figure S5. The Hall resistance is almost linear with little anomalous Hall effect (AHE) before reaching the quantum Hall regime. The absence of AHE could be related to the relatively weak spin-orbit coupling in the FePc/graphene heterostructure.

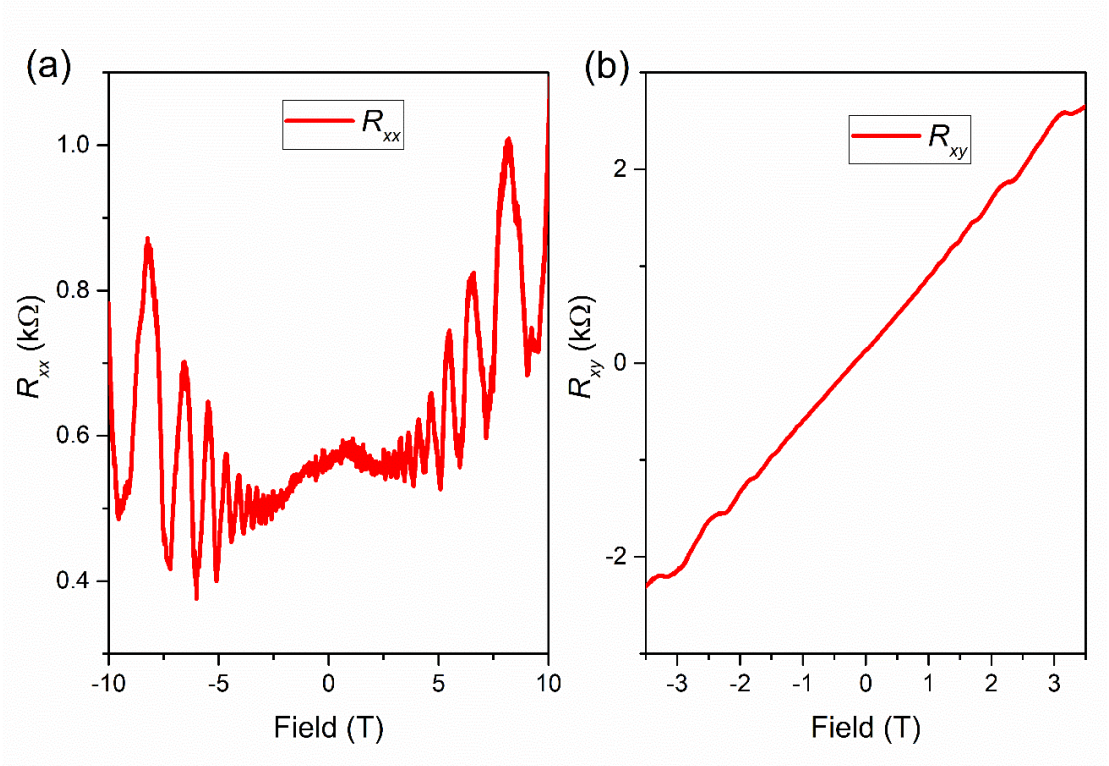

Figure S5 Magnetic field dependence of R_{xx} (a) and R_{xy} (b) of monolayer graphene covered by FePc film at 1.6 K.

Density-functional theory calculation of the graphene/FePc heterostructure

Figure S6 displays the density-functional theory calculation of monolayer graphene and FePc heterostructure (U = 3). According to the STM topography result, we use a close-packed FePc molecular place on the $6\times4\sqrt{3}$ graphene rectangular supercell. The Dirac cone emerges at the Γ point due to the band unfolding from the original K point in the hexagonal Brillouin zone of graphene primitive cell to the Γ point of the FePc graphene heterostructure. A mid-gap state within ±0.04 eV near the Fermi energy is presented in Figure S6, mainly contributed from the Fe 3d-orbital. The partial density of state calculation also shows a sharp peak originating from the Fe 3d orbital near the Dirac point (Figure S6-b).

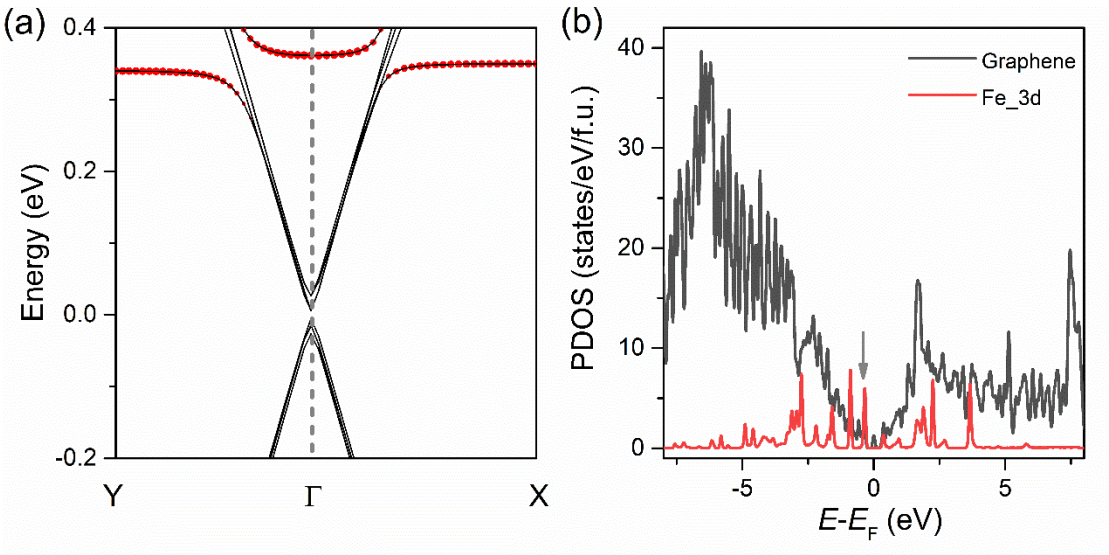

Figure S6 Density-functional theory calculation of the monolayer graphene/FePc heterostructure. (a) Band structure of FePc thin film on monolayer graphene. The red dots denote the contribution from the iron 3d-orbital. (b) Partial density of states of the heterostructure from graphene and the 3d orbital of iron. The gray arrow indicates the impurity state near Dirac point from the 3d-orbital of iron.

Our first-principles calculations within the density functional theory (DFT) framework were performed by the Vienna ab initio simulation package (VASP) based on the generalized gradient approximation of the Perdew-Burke-Ernzerhof (PBE) type and the projector-augmented-wave (PAW) pseudopotentials.[4-7] A rectangular form of FePc/Graphene supercell has been used to optimize the lattice structure. The energy cutoff was set to be 500 eV for the plane-wave basis. The Brillouin-zone integration was performed on a Γ- centered Monkhorst-Pack 6×5×1 k-point mesh, and we used a 15 Å vacuum layer between the surfaces to ensure that all the atoms are fully relaxed. The obtained lattice parameters are a = 14.8 Å, b = 17.1 Å.

The Ohmic versus nonlocal resistance in the bilayer graphene/FePc heterostructure

The Ohmic contribution to the nonlocal signal can be estimated from the Pauw formalism[8]

$$R_{Ohm} \approx \frac{1}{\pi}\rho_{xx}\left\{\ln\left[\cosh\left(\frac{\pi l}{w}\right)+1\right]-\ln\left[\cosh\left(\frac{\pi l}{w}\right)-1\right]\right\}$$

Where ρ_{xx} is the longitudinal resistivity, l and w are the length and width of Hall bar channel. Figure S7 shows that the ohmic contribution to the nonlocal signal is very weak.

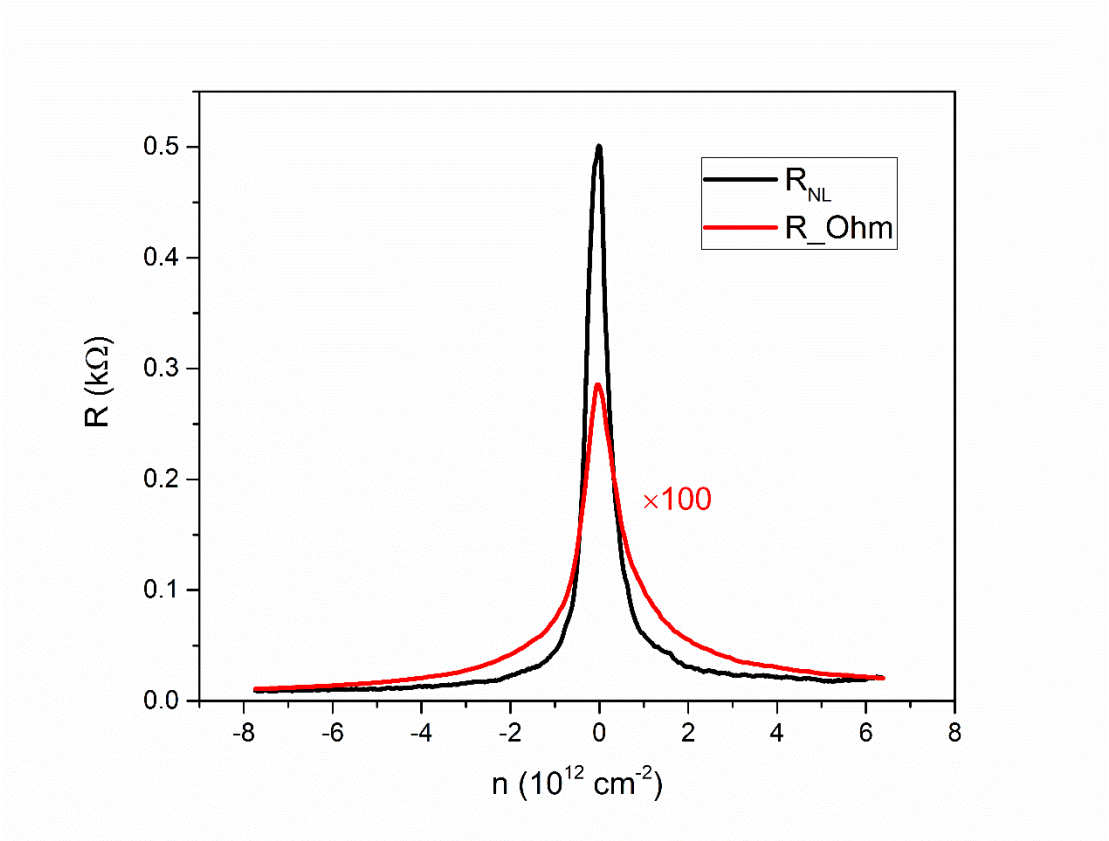

Figure S7 Comparison of the estimated Ohmic contribution and measured R_{NL} at 0 T. R_{Ohm} is magnified 100 times.

Temperature dependence of the nonlocal signal of the bilayer graphene/FePc heterostructure

Figure S8 shows the temperature dependence of $R_{NL,D}$ for the bilayer graphene/FePc heterostructure device. $R_{NL,D}$ experiences a slow-down transition at around 15 K.

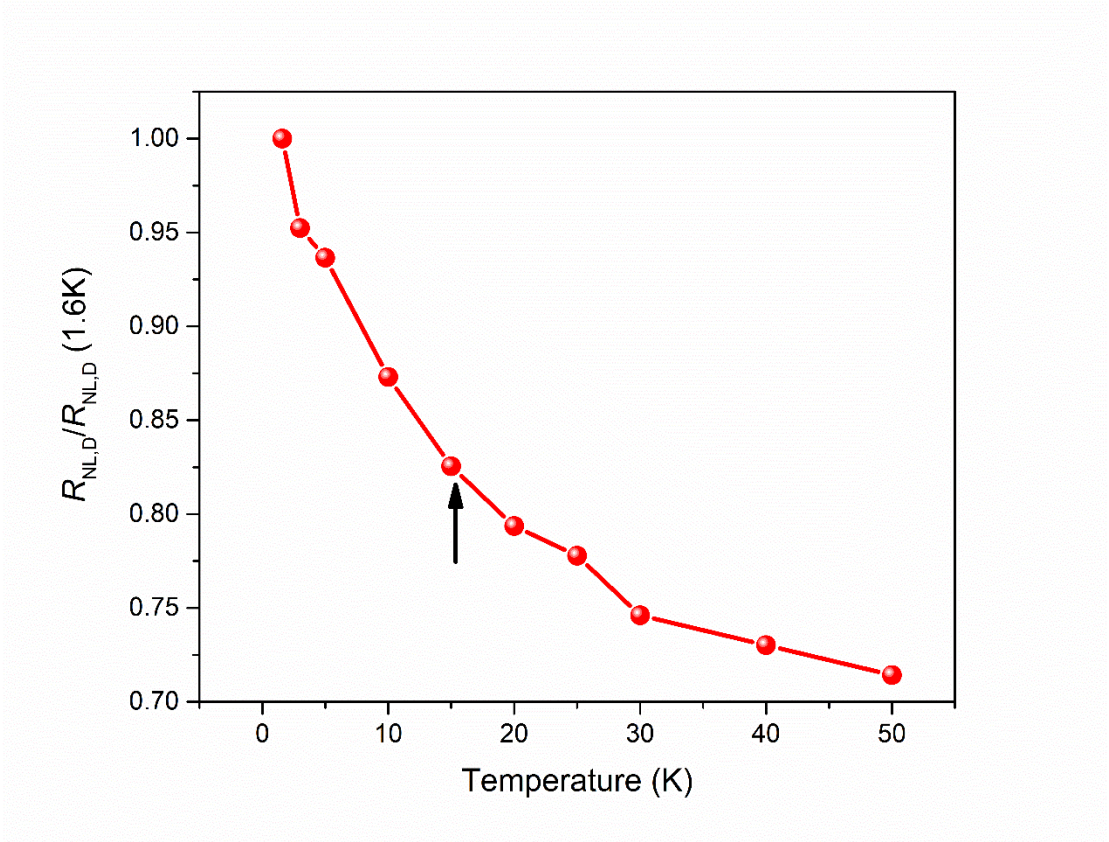

Figure S8 Temperature dependence of the $R_{NL,D}$ for the bilayer graphene/FePc heterostructure device. The black arrow indicates the occurrence of the transition.

Estimating the Zeeman splitting field of the bilayer graphene/FePc heterostructure

To estimate the strength of proximity exchange energy, we deduced the Zeeman splitting energy E_Z using the formula[9, 10]

$$E_Z = E_{Z0} \cdot \frac{\sqrt{(1+\mu^2 B^2)B_0^2}}{\sqrt{(1+\mu^2 B_0^2)B^2}} \times \frac{\sqrt{R_{nl,D}(B) - R_0}}{\sqrt{R_{nl,D}(B_0) - R_0}}$$

Where μ is the mobility, B_0 is the zero magnetic field, and R_0 is the nonlocal resistance at zero magnetic field. E_{Z0} is the Zeeman energy at the reference field $\mu_0 H_0$. For simple approximation, $E_{Z0} \approx g\mu_B \mu_0 H_0$ gives the lower bound of E_Z. By setting $\mu_0 H_0$ = 1 T, we can obtain E_Z = 0.5 meV and B_Z = 4.4 T for magnetic field $\mu_0 H$ = 2 T.

SdH oscillation and the calculation of quantum scattering time (τ_q) of the bilayer graphene device before and after FePc deposition

The SdH oscillation frequencies of the original and modified bilayer G/BN samples at various gate voltages are displayed in Figure S9. The higher harmonic frequency can be clearly seen in the frequency spectrum of the original graphene. After the deposition of FePc molecules, only the second higher harmonic frequency remained, whereas the other higher harmonic frequencies disappeared. The main frequency remained relatively the same.

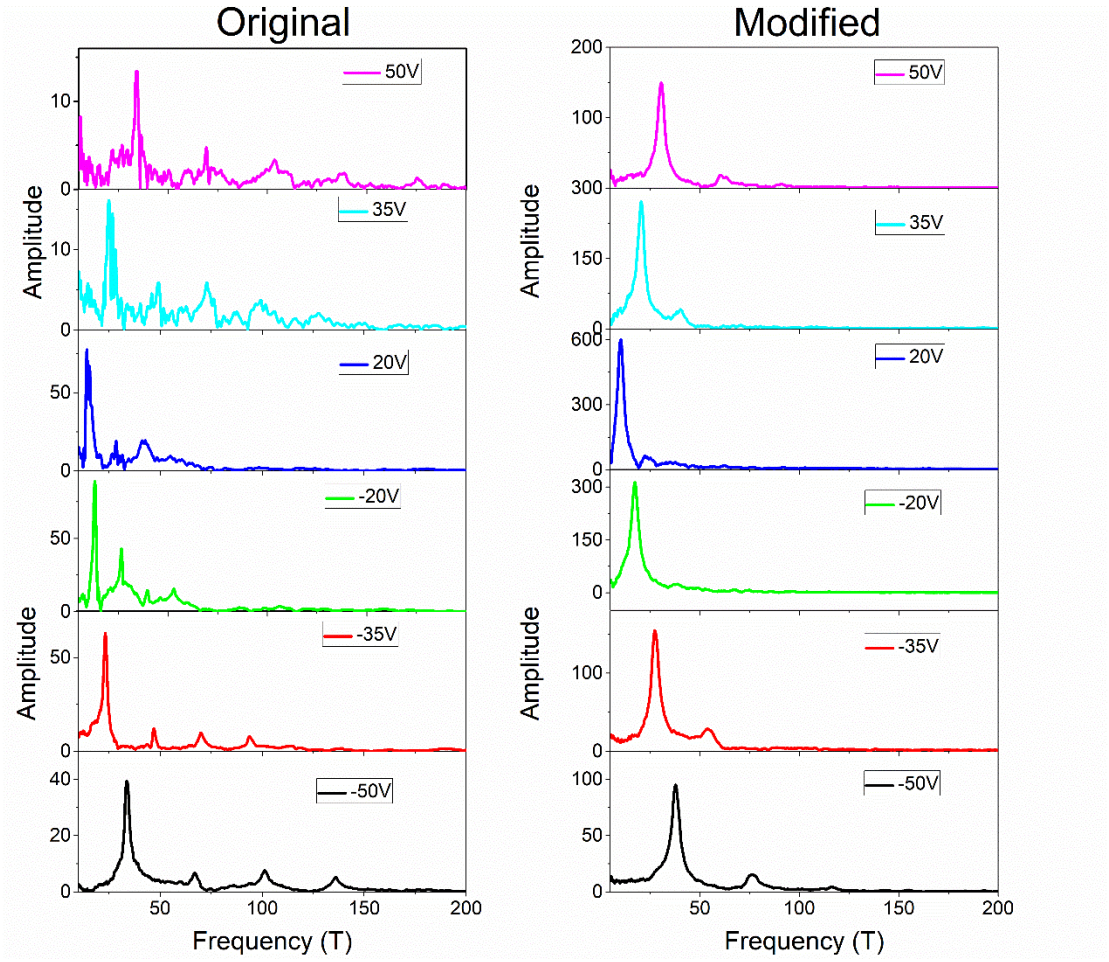

Figure S9 SdH oscillations frequency spectra of bilayer G/BN sample. (a) The original and (b) modified frequency spectra of bilayer graphene at different voltage gates.

The magnetoresistance at various gate voltages and temperatures was measured before and after FePc molecule deposition. Figure S10-a displays the bilayer G/BN sample's magnetoresistance at different temperatures when a -50 V gate voltage was applied. The fast Fourier transform (FFT) of the SdH oscillation results at different temperatures is shown in Figure S10-b. The FFT amplitude at different temperatures (Figure S10-c) was used to deduce the effective mass using the formula mentioned in the main text. Figure S11 displayed the obtained oscillation frequency and effective mass at various carrier density.

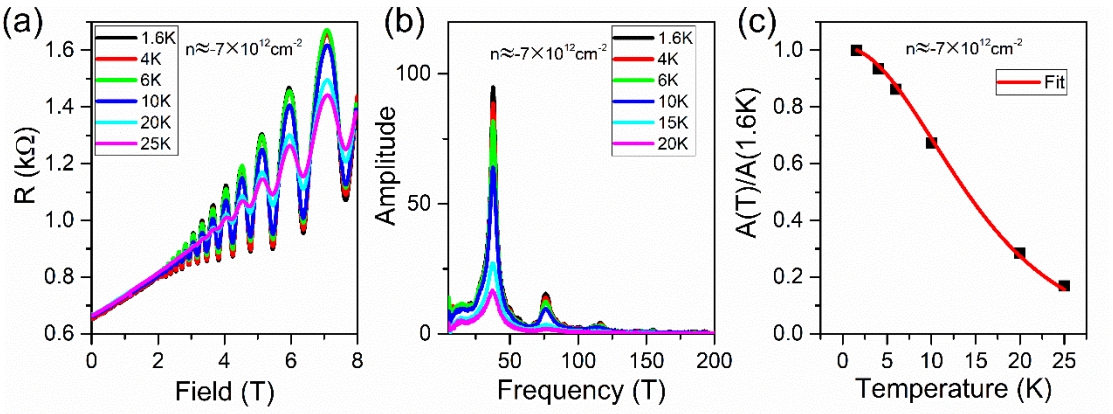

Figure S10 The magnetoresistance of bilayer G/BN sample at a fixed gate voltage of -50 V. (a) The magnetoresistance measured at different temperatures. (b) FFT amplitude of magnetoresistance results in (a). (c) Fitting of A(T)/A(1.6K) for the calculation of effective mass.

For both the electrons and holes, the m^* decreased as n decreased, which was consistent with the results of graphene on a SiO_2 substrate, revealing the non-parabolic nature of the energy bands.[2, 11] Before FePc deposition, the m^* of the original bilayer graphene sample on the electron side was comparable with the value of m^* on the hole side. However, m^* on the hole side surpassed that of the electron side after FePc deposition, indicating an enhanced electron-hole asymmetry. Besides, the values of effective mass for both the electron and hole sides decreased after FePc molecule deposition. The decrease in m^* could be related to the interfacial interactions from the FePc molecules. The quantum scattering time τ_q can be extracted from the

Dingle plot. The Dingle theory describes the oscillations amplitude ΔR_{xx} as

$$\Delta R_{xx} = 4R_0 e^{-\lambda_D}\lambda/\sinh(\lambda),$$

Where R_0 is the resistance at zero magnetic field and $\lambda_D = 2\pi^2 m^* k_B T_D/\hbar eB$. Here, $T_D = \hbar/2\pi k_B \tau_q$ is the Dingle temperature, where τ_q is the quantum scattering time. By linear fitting the inverse magnetic field dependence of $\ln[\Delta R_{xx}\sinh(\lambda)/4R_0\lambda]$, the value of λ_D can be obtained. Further, the value of τ can be deduced from λ_D .

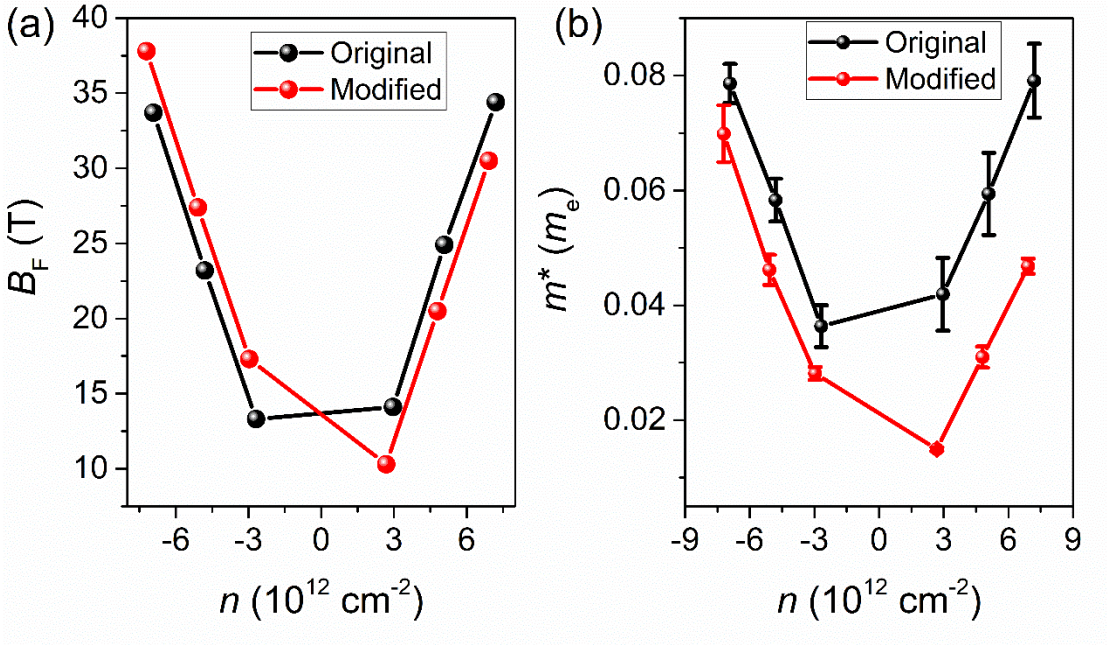

Figure S11 SdH oscillation analysis of bilayer G/BN sample before (original) and after (modified) FePc deposition. (a) The original and modified bilayer graphene oscillation frequency (B_F) versus carrier density, obtained from the SdH oscillation analysis. (b) The original and modified graphene effective mass versus carrier density, obtained from the SdH oscillation results measured at various temperatures.

References:

1. Doppagne, B.; Chong, M. C.; Lorchat, E.; Berciaud, S.; Romeo, M.; Bulou, H.; Boeglin, A.; Scheurer, F.; Schull, G., Vibronic Spectroscopy with Submolecular Resolution from STM-Induced Electroluminescence. *Physical Review Letters* **2017,** *118* (12), 127401.
2. Novoselov, K. S.; Geim, A. K.; Morozov, S. V.; Jiang, D.; Katsnelson, M. I.; Grigorieva, I. V.; Dubonos, S. V.; Firsov, A. A., Two-dimensional gas of massless Dirac fermions in graphene. *Nature* **2005,** *438* (7065), 197-200.
3. Hong, X.; Zou, K.; Zhu, J., Quantum scattering time and its implications on scattering sources in graphene. *Physical Review B* **2009,** *80* (24), 241415.
4. Kresse, G.; Hafner, J., Ab initio molecular dynamics for open-shell transition metals. *Physical*

Review B **1993,** *48* (17), 13115-13118.
5. Kresse, G.; Furthmüller, J., Efficient iterative schemes for ab initio total-energy calculations using a plane-wave basis set. *Physical Review B* **1996,** *54* (16), 11169-11186.
6. Kresse, G.; Joubert, D., From ultrasoft pseudopotentials to the projector augmented-wave method. *Physical Review B* **1999,** *59* (3), 1758-1775.
7. Perdew, J. P.; Burke, K.; Ernzerhof, M., Generalized Gradient Approximation Made Simple. *Physical Review Letters* **1996,** *77* (18), 3865-3868.
8. Wu, Y.-F.; Song, H.-D.; Zhang, L.; Yang, X.; Ren, Z.; Liu, D.; Wu, H.-C.; Wu, J.; Li, J.-G.; Jia, Z.; Yan, B.; Wu, X.; Duan, C.-G.; Han, G.; Liao, Z.-M.; Yu, D., Magnetic proximity effect in graphene coupled to a BiFeO3 nanoplate. *Physical Review B* **2017,** *95* (19), 195426.
9. Wei, P.; Lee, S.; Lemaitre, F.; Pinel, L.; Cutaia, D.; Cha, W.; Katmis, F.; Zhu, Y.; Heiman, D.; Hone, J.; Moodera, J. S.; Chen, C.-T., Strong interfacial exchange field in the graphene/EuS heterostructure. *Nature Materials* **2016,** *15* (7), 711-716.
10. Tang, C.; Zhang, Z.; Lai, S.; Tan, Q.; Gao, W.-b., Magnetic Proximity Effect in Graphene/CrBr3 van der Waals Heterostructures. *Adv Mater* **2020,** *32* (16), 1908498.
11. Zou, K.; Hong, X.; Zhu, J., Effective mass of electrons and holes in bilayer graphene: Electron-hole asymmetry and electron-electron interaction. *Physical Review B* **2011,** *84* (8), 085408.